Monitoring part-to-part gap and laser power effects in remote laser welding of 1050 aluminum busbar-to-terminal connections via optical microphone sensing

Optics & Laser Technology 192 (2025) 113494

Contents lists available at ScienceDirect

Optics and Laser Technology

journal homepage: www.elsevier.com/locate/optlastec

Monitoring part-to-part gap and laser power effects in remote laser welding of 1050 aluminum busbar-to-terminal connections via optical microphone sensing☆

Dario Basile [a,*], Rehab Al Botros [b], Manuela De Maddis [a], Valentino Razza [a], Pasquale Franciosa [b]

[a] DIGEP, Politecnico di Torino, Torino 10129, Italy
[b] WMG, The University of Warwick, Coventry CV4 7AL, UK

ARTICLE INFO

Keywords:
Laser beam welding
Membrane-free optical microphone
Part-to-part gap and laser power
Passing-through keyhole
Battery pack manufacturing

ABSTRACT

Advancements in membrane-free optical microphones have expanded their ability to detect acoustic signals up to tens of MHz, offering new possibilities for in-process monitoring of laser welding. Contributing to this growing field, this paper investigated part-to-part gap and laser power effects on weld events via optical microphone sensing. The study focused on remote laser welding of 1050 aluminum, representative of busbar-to-terminal connections. Acoustic emissions were collected and analyzed in the frequency domain using power spectral density calculations, identifying sound power as a critical signal feature. The findings reveal a strong correlation between the acoustic signals and the weld events, namely, lack of fusion, lack of connection, sound connection, and piercing. Notably, the adopted optical microphone effectively distinguished the transition from a blind to a passing-through keyhole, triggered by laser piercing, as well as the transition from lack of fusion to sound connections through lack of connection. These results demonstrated the potential of optical microphones for real-time, in-process monitoring of laser welding processes, thereby laying the groundwork for enhanced quality control of laser weldments.

1. Introduction

As the automotive sector transitions towards Battery Electric Vehicles (BEVs), advanced manufacturing processes are challenged by highly demanding functional and safety requirements. Being one of the most critical components of BEVs, the battery pack requires rigorous manufacturing standards to ensure both performance and safety [1]. The current consensus in industry is to use laser beam welding to join terminals and busbars due to the competitive welding speed and reduced heat input compared to other processes [2]. Manufacturing each battery pack involves thousands of connections, where even a single defective weld could compromise the safety and efficiency of the entire system [3]. This necessitates the development of novel monitoring strategies for in-process detection of defects to ensure the highest standards of quality and reliability [4]. A significant body of literature has addressed these needs with the development and testing of various in-process monitoring technologies. In general, the quality of laser weldments is assessed by measuring multiple features such as: (1) surface features (i.e., melt pool width, concavity, convexity); and, (2) subsurface features (i.e., weld depth, interface width, weld pores). Direct measurement of surface features is a well-established area and comprises of CMOS/CCD camera-based or laser-based sensors [5]. While multiple sensors can be installed on the same laser welding head to measure multiple features, direct measurement of subsurface features remains an unsolved problem. Subsurface features are ultimately what drive the functional performance of the weld, along with mechanical and electrical resistance as well as the durability. There have been few efforts in recent years to address in-process monitoring of subsurface features. Latest advancements in Optical Coherence Tomography (OCT) have shown promising results towards direct measurement of weld penetration depth [6]. The drawback of this approach is the need to recalibrate the monitoring system whenever a new set of process parameters is introduced. The sensitivity to changes of process parameters is mitigated by those sensors that passively observe the process emissions through monitoring of

☆ This article is part of a special issue entitled: 'LaserEMobility' published in Optics and Laser Technology.

* Corresponding author.
E-mail address: dario.basile@polito.it (D. Basile).

https://doi.org/10.1016/j.optlastec.2025.113494
Received 18 January 2025; Received in revised form 2 June 2025; Accepted 21 June 2025
Available online 10 July 2025

optical emissions. For example, Chianese [7] demonstrated that part-to-part gap and laser power variations can be diagnosed by observing changes in the process light (from ultraviolet to the visible spectrum). A complementary approach is to monitor acoustic emissions. Acoustic emissions capture process-intrinsic phenomena generated by the rapid thermal and mechanical changes within the weld zone. However, its effectiveness has been limited by the high sensitivity to the background noise, making it challenging to isolate relevant weld features [8]. The recent development of optical microphones, capable of detecting a broad frequency range up to several MHz, has renewed interest in this area, as their operating principle may offer improved resilience to background noise under certain conditions [9].

This acoustic transducing approach, working entirely without a vibrating membrane, relies on detecting changes in the refractive index within a rigid Fabry-Pérot interferometric cavity rather than mechanical vibrations of a diaphragm. This design eliminates resonance-induced noise artifacts common in conventional microphones. Additionally, it provides an exceptionally broad frequency range, from 10 Hz to several tens of MHz (notably beyond human hearing, which spans 20 Hz to 20 kHz), thus enabling clear spectral separation between valuable acoustic signals generated during welding and unwanted noise [10]. Thanks to its compact sensor head, the optical microphone can be positioned close to the process zone, minimizing interference from distant background noise. The principle of operation, schematically shown in Fig. 1, involves directing a measurement laser into a small cavity formed by two parallel semi-reflective mirrors. Acoustic emissions (AE) from the welding process induce pressure variations, altering the refractive index inside the cavity. These changes in the refractive index modulate the intensity or phase of the reflected light, which is detected by a photodiode and converted into an electrical signal corresponding to AE.

AE consist of transient elastic waves generated within a material due to rapid, localized energy release, often linked to structural changes or defects. In laser welding, various complex phenomena occur simultaneously, such as rapid vaporization, keyhole formation, and plume dynamics, each significantly contributing to the generation of distinct acoustic signatures [8]. The keyhole's dynamic behavior, characterized by continuous oscillation, fluctuations in size, and periodic collapse, is the primary source of acoustic emissions. Pressure waves emanate directly from these rapid keyhole movements and propagate through the surrounding medium, generating characteristic AE [11]. Although keyhole oscillation frequencies depend on specific material and process parameters, they are consistently reported in the low kHz range. For example, theoretical models predict eigenfrequencies near 1.5 kHz, while experimental data show frequencies between 4–10 kHz [11]. Geiger et al. [12] observed a dominant frequency at approximately 3 kHz. Volpp et al. [13] measured pressure oscillations between 1 and 4 kHz, with higher frequencies for top-hat beam profiles. Recent high-speed X-ray imaging revealed dominant keyhole aperture oscillation frequencies around 0.85 kHz [14]. It is important to note that while keyhole oscillations exhibit distinct frequencies, those detected by a microphone depend on the coupling mechanism, resonance conditions, material properties, and boundary effects. As highlighted by Luo et al. [15], strong AE occurs only when the keyhole geometry and pressure conditions support resonance, such as when the keyhole closely approximates a resonant cavity (e.g., a Helmholtz resonator or an open-closed tube) and the oscillation frequency matches the cavity's natural resonance. In addition to keyhole-driven emissions, the weld plume significantly contributes to AE generation. It exerts recoil forces on the molten pool surface and experiences rapid thermal expansion and contraction, producing additional AE [16]. Moreover, as suggested by the Bastuck's model, AE during laser beam welding can also originate from surface evaporations. This includes localized boiling and vaporization of the material surface. High-frequency acoustic emissions (>200 kHz) can also arise from rapid phase transitions, such as microstructural changes during rapid solidification [17]. As a result, AE signals do not always directly represent intrinsic physical events but instead reflect a convolution of these intrinsic emissions with resonance phenomena. This complexity makes the study of AE in laser welding challenging and indicates the need for further investigation.

Table 1 reports the summary of the key contributions where optical microphones have been used for monitoring of laser-material processing. Notably, optical microphones have been successfully used for laser-based additive manufacturing (AM) processes. Nasab et al. [18] investigated the acoustic signatures of instabilities during laser melting in Laser Powder Bed Fusion (LPBF) by utilizing an optical microphone. The study revealed that acoustic signals in the 40–82 kHz range effectively indicated shifts from conduction to keyhole regimes. De Formanoir et al. [19] employed an optical microphone to monitor AE during laser beam re-melting in LPBF, aiming to control porosity. Their analysis identified distinct acoustic signatures in the 30–100 kHz range that correlated with

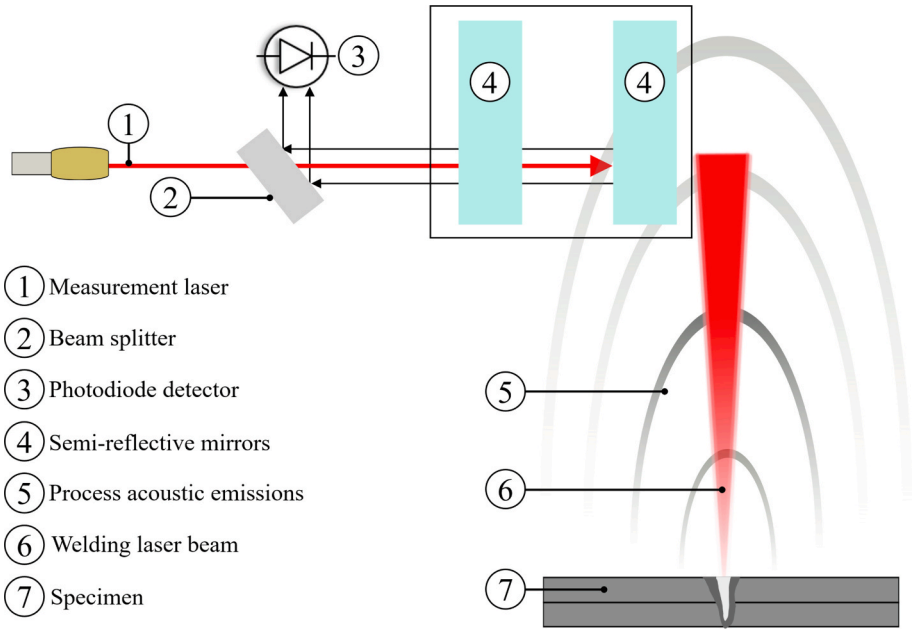

Fig. 1. Schematics (not in scale) of the optical microphone based on the Fabry-Pérot interferometer.

Table 1
Key research contributions using optical microphones in laser-material processing.

Material	Application	Detected weld feature (significant AE frequencies)	Ref.
AISI 304 stainless steel	Laser Powder Bed Fusion (LPBF)	Inter-regime instabilities (40, 60, 70, 77, 82, 250 kHz)	[18]
316L stainless steel	Laser Powder Bed Fusion (LPBF)	Porosity (30–100 kHz)	[19]
316L stainless steel, tool Steel M2	Laser Metal Deposition (LMD)	Cracks (>350 kHz)	[20]
Polyimide-coated Cu	Laser ablation	Layer transitions (100–2000 kHz)	[22]
Cu, Polyimide	Laser ablation	– Layer transitions (50–2000 kHz) – Ablation volume (50–2000 kHz)	[21]
Carbon-based Diffusion Media	Laser ablation	– Focus position (97,5–98.5 kHz) – Ablation volume (50 kHz)	[29]
316L stainless steel, TA6V Ti	Laser welding	Penetration depth(40–90 kHz)	[9]
Cu-OF	Laser welding	– Spatters (10–800 kHz) – Detection of laser beam deviations (10–800 kHz)	[24]
Cu	Laser welding	Penetration depth (40–90 kHz)	[28]
Cu,Ni-plated Steel	Laser welding	– Penetration depth (N.A.) – Surface contamination (N.A.) – Gap (N.A.)	[25]
316L stainless steel	Laser welding	– Burn-through (N.A.) – Gap (N.A.) – Connection status (N.A.) – Humping (N.A.) – Surface contamination (N.A.) – Focus position (N.A.)	[27]
Ni	Laser welding	Contamination (50–175 kHz)	[26]

successful pore removal. Prieto et al. [20] investigated crack detection with an optical microphone for Laser Metal Deposition (LMD) process. Acoustic emissions in the 350–1000 kHz range were correlated with the occurrence of crack formation. In addition to AM processes, optical microphones have also been explored for ultra-short pulse (USP) laser ablation processes, where rapid material transitions and layer differentiation demand high temporal and spectral resolution. Lutz et al. [21,22] used an optical microphone to monitor a USP laser ablation of multi-layer materials. By analyzing acoustic energy across the 100–2000 kHz range, the study identified clear increases in signal corresponding to transitions between copper and polyimide layers. Geiger et al. [29] employed an optical microphone to monitor focus position, pulse repetition rate, and drilling depth during USP laser processing of fuel cell diffusion media. They observed correlations between these parameters and variations in acoustic emissions within the 50–200 kHz range. A few contributions have been made toward monitoring the laser welding process. An interesting study from Krämer et al. [23] showed how the positioning of the optical microphone affected the detectability of weld features during deep penetration laser welding. The study varied the distance, angle, and orientation relative to the working surface and analyzed signals across frequencies up to 250 kHz. The results indicated that positioning the sensor at a flat angle relative to the sample surface significantly enhanced signal strength above 10 kHz. Omlor et al. [24] combined an optical microphone and high-speed camera to monitor the quality of hairpin welding in electric motor stators by analyzing AE. Regression analysis showed that AE in the 10–800 kHz frequency range were well-explained by laser power ($R^2 = 0.805$) and focus position ($R^2 = 0.835$). Heilmeier et al. [25] investigated the influence of surface contamination and workpiece misalignment on AE. The study revealed distinct changes in statistical features when defects such as surface contamination and misalignment were introduced. Similarly, Krämer et al. [26] used an optical microphone to detect the presence of surface contamination during T-joint laser welding. Significant changes in AE were observed in the 50–175 kHz range, correlating with increased porosity, seam underfill, and reduced welding depth. Weiss et al. [27] used an optical microphone to detect burn-through, humping, and lack of fusion during laser beam welding of thin stainless-steel foils, achieving a 94.78 % classification accuracy after applying a denoising procedure and extracting time and frequency-domain features. Some studies have also used optical microphones to monitor weld penetration depth. Authier et al. [9] combined an optical microphone with OCT for real-time measurement of keyhole depths. Acoustic signatures within the 40–90 kHz range showed a strong correlation with welding penetration depth, with R^2 values reported up to 0.9928. A material-independent peak around 60 kHz was observed and associated with the keyhole opening event. Similar results were obtained by Tomcic et al. [28] who used an optical microphone to monitor weld depth during laser welding of copper. Among 17 extracted acoustic features, the zero-crossing rate, particularly within the 40–90 kHz range, was consistently ranked as one of the most informative predictors of weld depth across all regression models.

The reported studies demonstrate that optical microphones are gaining significant attention in the field. This also highlights the need for further research to establish standardized methodologies and expand their applicability to different materials, process parameters, and industrial settings. Contributing to this growing field, this paper pursues two main objectives: first, to explore the relationship between AE and weld features in the presence of part-to-part gaps and varying laser power; and second, to investigate whether the transition from a blind to a passing-through keyhole can be correlated with changes in airborne sound emissions. This is particularly relevant in battery cell production, where an undetected passing-through keyhole can result in cell puncture, posing significant safety risks. Undetected punctures can indeed lead to catastrophic events, such as electrolyte leakage and, in more severe cases, fire and thermal runaway after a few recharge cycles during battery operation [30]. Although this issue is widely acknowledged, there has been no significant published research addressing in-process monitoring using optical microphones.

2. Materials and methods

2.1. Welding configuration and setup

The specifications of the welding equipment are reported in Table 2 with the experimental setup in Fig. 2. The material used in this work was aluminum 1050. The dimensions of the specimens were 120 (length in X) × 38 (width in Y) × 1 (thickness in Z) mm. Experiments were conducted in an overlap configuration, and the weld length was 30 mm in the X direction. The laser source was the Coherent HighLight FL-ARM 10000, having 100 μm core fiber diameter. Although the source can generate a combined core-to-ring beam, only the core laser was implemented for this study. The laser beam was delivered by a Scout-200 2D

Table 2
Specifications of the laser welding system.

Coherent HighLight FL-ARM 10,000		K-lab SCOUT-200	
Maximum power	10 kW	Maximum allowed power	2 kW
Core maximum power	5 kW	Scanning field	70 x 70 mm^2
Wavelength	1070 ± 10 nm	Collimating length	100 mm
Fiber core diameter	100 μm	Focusing length	254 mm
Beam Product Parameter (BPP)	4 mm·mrad	Rayleigh length	0.8 mm
Laser mode	Multi-mode	Spot size	254 μm

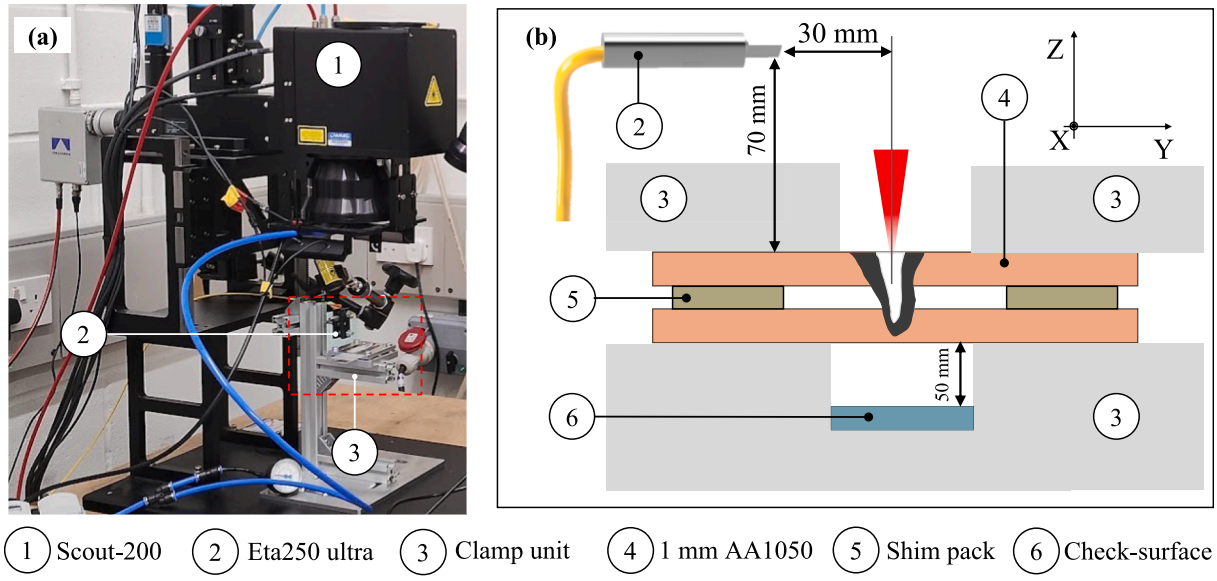

Fig. 2. (a) Laser welding and sensor setup; (b) schematic view of the fixture setup and positioning of the optical microphone.

scanner (Laser and Control K-lab, South Korea).

All the experiments were performed without shielding gas and without filler wire. The focal point was set on the upper surface of the upper sheet, obtaining a 254 μm spot size. A cross-jet was not utilized in this study, as its inclusion would have introduced additional variables requiring further filtering and analysis. This was motivated by the fact that the primary objective of the research was to study the effect of laser power and part-to-part gap on acoustic emissions, isolating these factors without the potential disturbances that a cross-jet might introduce. Samples were wiped with acetone before welding to remove any surface contamination.

The laser welding process was monitored using an Eta250 ultra optical microphone (Xarion, Austria). The microphone was placed 70 mm above the weld zone (Z-direction) and 30 mm laterally from the beam path (Y-direction), with its sensing face oriented toward the laser-material interaction area. This positioning was chosen based on preliminary trials to ensure sufficient signal amplitude while minimizing the risk of direct exposure to the laser beam or weld spatters. All tests were performed with the microphone in this fixed position and orientation to ensure experimental consistency. The influence of sensor positioning on signal strength has already been addressed in the literature [23]. To synchronize the acoustic signals with the laser welding process, an MSO3014 oscilloscope (Tektronix, Oregon) was employed. The analog signal sent from the 2D scanner to the laser source served as the primary trigger. Upon detection, the oscilloscope triggered the sensor control unit (SCU) of the microphone, initiating the recording of acoustic emissions. The microphone signals were acquired at a sampling frequency of 2.5 MHz, with a total of 5 million data points collected. According to the Nyquist-Shannon theorem [31], this allowed for a total recording time of 2 s and a maximum detectable frequency of 1.25 MHz.

2.2. Design of experiments and weld characterization

A full factorial design was employed to systematically evaluate the effects of laser power and part-to-part gap on the acoustic emissions captured by the optical microphone. It is worth noting that this paper does focus on assessing the optical microphone's ability to detect defects, rather than achieving optimal weld quality. Therefore, the levels of laser power and part-to-part gap were selected accordingly. Laser power (P_L) was varied in the range of 800–1350 W in 50 W increments and the part-to-part gap was varied in the range of 0–1 mm in 0.25 mm increments (see Table 3). Each combination of parameters in the full factorial matrix was replicated three times, resulting in a total of 180 welding trials.

Table 3
List of process parameters varied in the welding trials.

Parameters	Unit	Value
Laser Power, P_L	W	800, 850, 900, 950, 1000, 1050, 1100, 1150, 1200, 1250, 1250, 1300, 1350
Part-to-part gap	mm	0, 0.25, 0.5, 0.75, 1.0

In addition to the factorial combinations, a separate set of tests was conducted at 2000 W with zero part-to-part gap, specifically to investigate the occurrence of the piercing event. This power level was determined experimentally as the threshold at which the laser beam fully penetrated the bottom sheet, marking a clear transition from a blind to a passing-through keyhole. These tests at 2000 W were replicated three times to ensure the repeatability of the observations. It is worth noting that a fully penetrated weld does not imply necessary a piercing event. Looking at Fig. 3(a–b) it appears that both cases represent full-penetration welds (molten layer fully extended throughout the bottom surface). However, the case in (a) has a blind keyhole, which does not propagate throughout the bottom sheet. As such, the laser beam (shown as small arrows in Fig. 3(a–b)) is eventually only absorbed by the keyhole walls (or back-reflected towards the top) and does not pierce through the bottom. Following this logic, only case (b) is associated with a piercing event. To determine experimentally the piercing event, a stainless-steel foil, labeled "check-surface" in Fig. 2(b), was placed 50 mm below the bottom sheet. The choice of a 50 mm distance was based on a representative battery module design, accounting for the spacing between the busbar and the cells, as well as the presence of any plastic harnesses securing the busbar. If the laser had pierced the bottom sheet, a marking would have appeared on the stainless-steel foil. While piercing occurred at 2000 W under the tested conditions, this threshold is not assumed to be universal. Piercing could depend on additional factors such as material properties, optical configuration, and other process parameters. Future research should explore whether piercing caused by different process conditions can be detected using the same testing approach.

Shim packs (Meusburger, Germany) of 12.5 mm width were employed to precisely control part-to-part gaps. To ensure a consistent laser beam spot size and thus maintain a constant power density, the

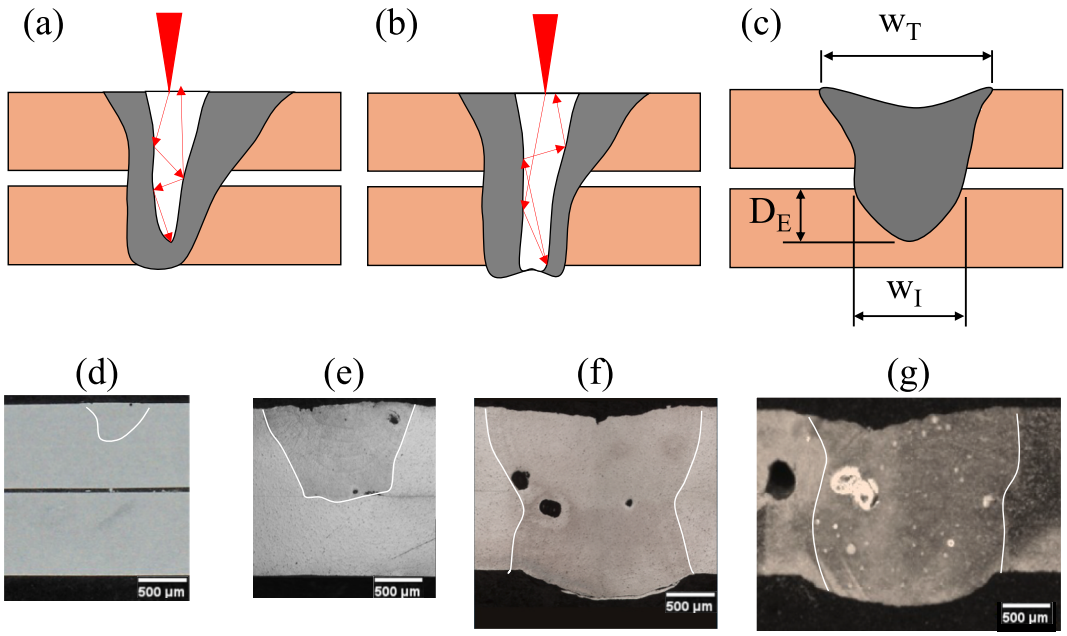

Fig. 3. (a, b) Conceptual representation of the transition from a blind to a passing-through keyhole; (c) schematics of the weld features; representative weld (at zero part-to-part gap) of (d) lack of fusion, (e) lack of connection, (f) sound connection, (g) weld where piercing occurred.

focal position in Z was adjusted by an amount equal to the shim pack used in each welding configuration. All welds were produced with a wobbling pattern of 0.2 mm radius at 1 kHz frequency (list of constant parameters is in Table 4).

Metallographic analysis was conducted by cutting each seam into two cross-sections, with a 10 mm distance from both the start and the end of the weld. The cross-sections were then hot-mounted, grinded, polished, and etched with a 20 % NaOH solution. Pictures of the cross-sections were taken with the Nikon Eclipse LV150N. Cross-sections of the welded samples were examined, and the following weld features were extracted (see Fig. 3(c)): weld width at the top of the weld bead (W_T); weld width at the interface between the two sheets (W_I); and, effective penetration depth, measured from the top of the bottom sheet to the lowest point of the weld (D_E). D_E was used as a key geometrical feature to evaluate the effectiveness of the connection between the upper and the bottom sheet. In this study, the weld connection was considered effective when D_E exceeded 25 % of the thickness of the lower sheet. The acceptance limit on D_E has been adapted from previous studies [32,33]. Four events were introduced (Fig. 3(d−g)):

- *Lack of fusion*: no significant fusion was achieved in the upper sheet, and only a superficial marking was observed.
- *Lack of connection*, associated with either: (1) effective weld depth, D_E, lower than 25 % of the sheet thickness (1 mm), indicating insufficient penetration; or, (2) full penetration through the bottom sheet, but lack of material bridging due to large part-to-part gap.
- *Sound connection*: good weld with D_E greater than 25 % of the sheet thickness (1 mm), and not exceeding the threshold for a piercing event (marking on the "check-surface), indicating an acceptable connection between the sheets; and,
- *Piercing event*: visible mark left on the "check-surface".

Table 4
Constant welding process parameters.

Parameters	Unit	Value
Welding speed	mm/s	15
Wobbling trajectory	–	Circular
Wobbling frequency	kHz	1
Wobbling radius	mm	0.2
Seam length	mm	30

2.3. Signal processing

Preliminary tests were conducted to evaluate the impact of the background noise (ventilation hood, water circuit, compressed air circuit) on the acoustic signal captured by the microphone. The Signal-to-Noise Ratio (SNR) was calculated to quantify the level of noise interference. The SNR was determined as in Eq. (1), where RMS_{signal} represents the root mean square of the captured acoustic signal and $RMS_{background}$ is the root mean square of the background noise.

$$SNR = 20\log_{10}\left(\frac{RMS_{signal}}{RMS_{background}}\right) \quad (1)$$

Three denoising techniques, namely wavelet denoising, spectral subtraction, and Wiener filtering, were selected based on their common use in non-stationary signal environments such as acoustic emissions [27,34,35]. Each method was applied to the same Region Of Interest (ROI) of the signal, and the resulting SNR values were compared. The original raw data yielded an SNR of approximately 17.93 dB, indicating minimal interference from background noise. Spectral subtraction and wavelet denoising maintained the SNR at 17.93 dB, while Wiener filtering reduced it to 14.49 dB. This outcome indicates that the noise and the signal of interest are likely to share overlapping frequency bands. Attempts to suppress the noise, therefore, involve the risk of affecting the signal of interest. The reduced SNR observed with the Wiener filter supports this hypothesis, as its algorithm inherently balances noise suppression against preserving signal fidelity [36]. Consequently, the initial recording setup proved effective for capturing acoustic emissions without introducing significant background noise interference. Although the recorded signals demonstrated an SNR of 17.93 dB in a controlled laboratory setup, actual production floors often involve additional background noise from other machinery and auxiliary equipment. Furthermore, although cross-jet flow was intentionally excluded in this paper to isolate the roles of part-to-part gap and laser power, introducing cross-jet may alter the noise spectrum and should be investigated in subsequent studies.

Fig. 4 shows a typical microphone-based signal and the output analog signal of the laser source. Notably, after a ramp-up phase of 7 ms

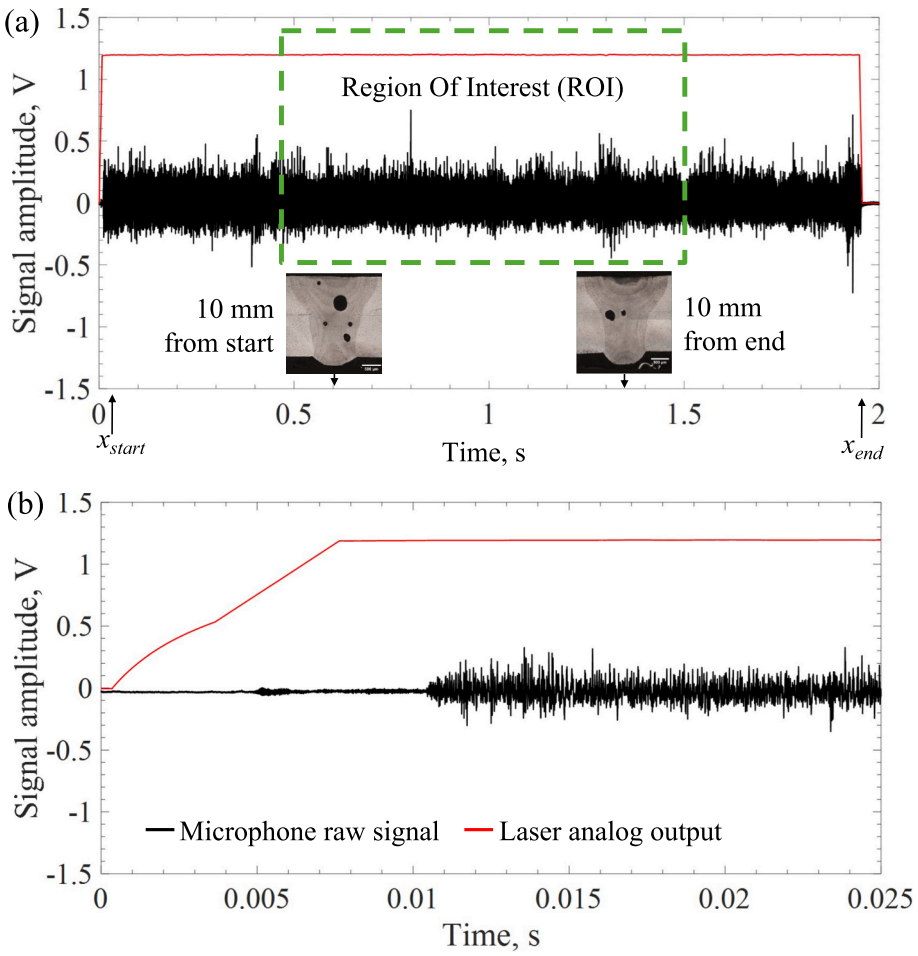

Fig. 4. (a) Example of optical microphone raw signal and analog signal of the laser output; (b) zoom-in view between 0 to 0.02 s to highlight the delay between the laser output and the acoustic signal.

(Fig. 4(b)) the laser analog signal does reach its maximum value (1 V equivalent to 1000 W). The microphone starts recording the acoustic signal at 11 ms, indicating a delay of 4 ms between the laser reaching its peak power and the actual recording of the acoustic emissions. This delay is attributed to the time required for the laser to transfer sufficient energy to the material for it to reach its melting point. The process is not instantaneous because it involves thermal diffusion, where heat propagates through the material's volume. To focus the analysis on the steady-state phase of the welding process, rather than any initial transitory effects, only the central portion of the acoustic signal (between 0.5 and 1.5 s) was extracted. This corresponded to the selected ROI, comprised of the specimen cross-sections evaluated at 10 mm (0.66 s) and 20 mm (1.33 s) from the start, ensuring that these regions were included within the analyzed portion of the signal.

Fig. 5 shows the methodological flowchart of the procedure implemented for signal processing. Starting from the raw signal x(t) within the ROI, the Discrete Fourier Transform (DFT), X(f), is computed; and, then the Power Spectral Density (PSD) is evaluated to analyze the frequency characteristics. PSD represents the power of a given signal distributed across different frequencies, allowing to down-select the dominant frequency components.

Welch's method was employed to compute the PSD because it reduces noise by averaging overlapping segments of the signal [37]. The PSD was computed using the Hann window [38] and is given in Eq. (2),

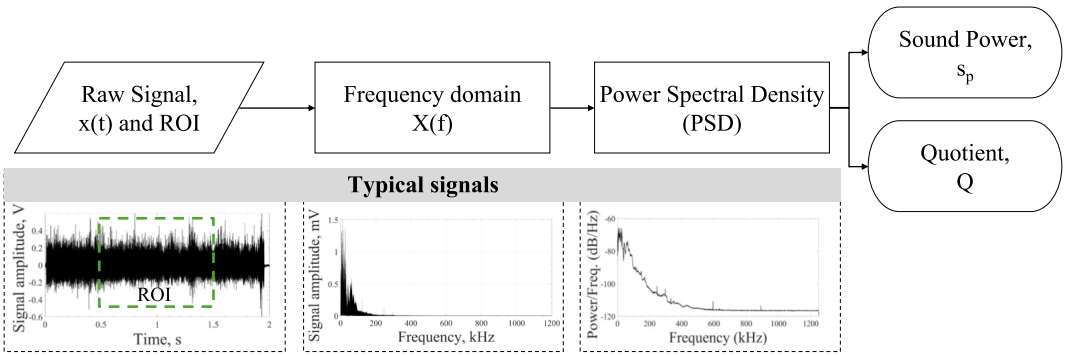

Fig. 5. Methodological flowchart of the procedure implemented for signal processing.

where $X_i(f)$ is the DFT of the i-th segment of the signal; L is the number of overlapping segments and U is a normalization factor accounting for the windowing function applied to each segment (U ≈ 0.375, for Hann window).

$$P_{xx}(f) = \frac{1}{L \bullet U}\sum_{i=0}^{L-1}|X_i(f)|^2 \quad (2)$$

A window length of 4 ms (corresponding to 10,000 samples at a 2.5 MHz sampling rate) and an overlap of 2 ms were chosen for the computation of the power spectral density (PSD) using Welch's method. This configuration provides a frequency resolution of 250 Hz, which is sufficient to capture the relevant frequency content of the acoustic emissions while ensuring a detailed spectral representation. A 50 % overlap was employed to improve the statistical reliability of the PSD estimate through averaging, without introducing excessive computational redundancy. These parameters were validated through preliminary tests to ensure they preserved the signal characteristics while minimizing spectral leakage and variance.

Two features were then extracted from the PSD:

- *Total sound power*, s_p, expressed as in the Eq. (3), obtained by the integration across all the frequencies, [f_{min}-f_{max}]. In this study, the 0–1.25 MHz frequency range was used (corresponding to the maximum detectable frequency based on the 2.5 MHz sampling rate, according to the Nyquist–Shannon theorem [31]); and
- *Quotient* of the PSD, *Q*, calculated to compare the spectral differences between two signals from two different welding conditions. This approach provides a measure of how PSD diverges across the frequency spectrum, highlighting regions where acoustic emissions differ significantly [36]. The quotient *Q* between two spectra, PSD_1 and PSD_2, is computed as in the Eq. (4).

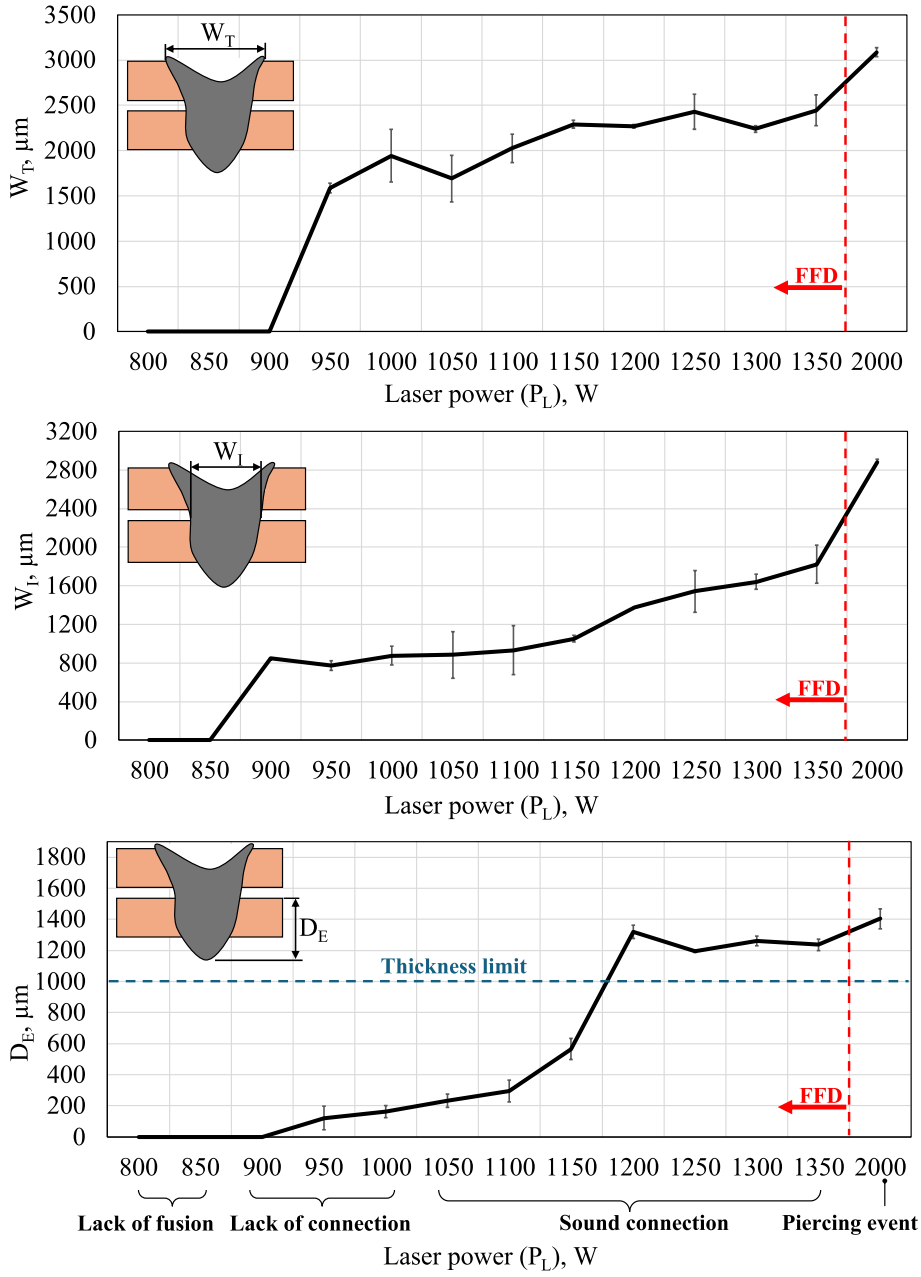

Fig. 6. Results of metallographic analysis at zero part-to-part gap. Pearson's correlation coefficients between P_L and the weld features are 88% (W_T), 95% (W_I), and 93% (D_E). "FFD" indicates the process window tested by the full factorial design.

$$s_p = \int_{f_{min}}^{f_{max}} P_{xx}(f)\, df \tag{3}$$

$$Q = 10\log_{10}\left(\frac{PSD_2(f)}{PSD_1(f)}\right) \tag{4}$$

The correlation between signals was quantified by the Pearson's correlation coefficient. The value of the correlation ranges from −100 % to 100 %, where 0 indicates uncorrelated signals. A 2-way Analysis-Of-Variance (ANOVA) analysis was implemented to test the statistical significance of the process parameters against the signals – the significance level set at 5 %.

3. Results and discussion

Results are presented to firstly discuss the individual effect of laser power at zero part-to-part gap. Subsequently, the combined effect of laser power and part-to-part is introduced.

3.1. Variation of laser power at zero part-to-part gap

Fig. 6 illustrates the variation of the weld geometrical features as a function of laser power (P_L) at zero part-to-part gap. At P_L below 850 W, no melting occurred with only surface marking on the upper sheet. Between 900 and 1000 W, melting was observed in the upper sheet, but the weld resulted in lack of connection. Specifically, at 900 W, no melting of the bottom sheet was observed, whereas at 950 W, melting of the bottom sheet started, although it was still insufficient to form a sound connection. Sound connections were instead achieved in the range 1050–1350 W. Laser piercing occurred at P_L = 2000 W, resulting in a significant increase in weld width at the interface (W_I) and excessive penetration depth (D_E).

Fig. 7 shows the variation of total sound power (s_p) with increasing laser power (P_L) at zero part-to-part gap. At P_L = 850 W, the sound power remains very low, corresponding to a lack of fusion's event. At P_L = 900 W, a sharp increase in acoustic emissions signifies the initiation of melting in the upper sheet, despite the absence of a sound connection. From 1000 W to 1050 W, a further increase in sound power is observed, reflecting the transition from lack of connection to sound connection. Between 1050 W and 1350 W, the sound power continues to increase, albeit more gradually. This trend reflects a more stable welding regime where the connection between the two sheets is maintained and no significant change in weld regime is expected. These results are also confirmed by previous findings in the literature [9,28]. A pronounced jump in s_p is observed at P_L = 2000 W. Despite the relatively modest changes in s_p between adjacent power levels, a strong positive correlation (95 %) was observed between s_p and the laser power (P_L), which is further reflected in the variations of the geometrical features (Fig. 6).

The overall trend is consistent with the expectation that higher laser power induces more pronounced AE due to increased energy transfer to the material. To further analyze the spectral differences in acoustic emissions between distinct welding regimes, PSD quotients (Q) were calculated between pairs of representative weld conditions. Three power levels were selected, 850 W, 950 W, and 1050 W, corresponding to the key weld conditions identified through metallographic analysis: lack of fusion (850 W), lack of connection (950 W), and sound connection (1050 W). The first PSD quotient was calculated between laser power levels of P_L = 850 W and P_L = 950 W, shown in Fig. 8 (a). At P_L = 850 W, the interaction is limited to superficial marking, with no melting and minimal acoustic activity. In contrast, P_L = 950 W initiates melting of the upper sheet, even though no sound connection is achieved. This transition activates key physical mechanisms, such as vaporization, molten pool oscillations, and plume dynamics. This results in a broader and more intense acoustic response. The PSD quotient highlights this shift clearly, especially in the 0–400 kHz range, with differences reaching up to 31 dB.

Another PSD quotient was evaluated between P_L = 950 W (PSD_1) and P_L = 1050 W (PSD_1) and is shown in Fig. 8(b). For better readability, a horizontal line at zero dB was drawn, indicating no difference between the two spectra. A positive Q value ($PSD_2 > PSD_1$) suggests that the frequency contribution of PSD_2 is higher compared to PSD_1. Conversely, a negative Q value ($PSD_2 < PSD_1$) indicates a lower frequency contribution in PSD_2 compared to PSD_1, suggesting reduced acoustic emissions.

At P_L = 950 W, as previously mentioned, both sheets melted, but insufficient penetration was reached. In contrast, at P_L = 1050 W, a sound connection was achieved. Within the 0–400 kHz range, the difference in dB is generally smaller than in the previous comparison (Fig. 8 (a)), with a maximum value of 3.2 dB. This suggests that this frequency band carries information related to the level of penetration depth. Three notable peaks are observed at 8 kHz, 63 kHz, and 110 kHz. The peak at 63 kHz falls within a frequency range commonly associated with keyhole penetration and has previously been attributed to the onset of stable keyhole formation [9,18,28]. In our study, the appearance of a

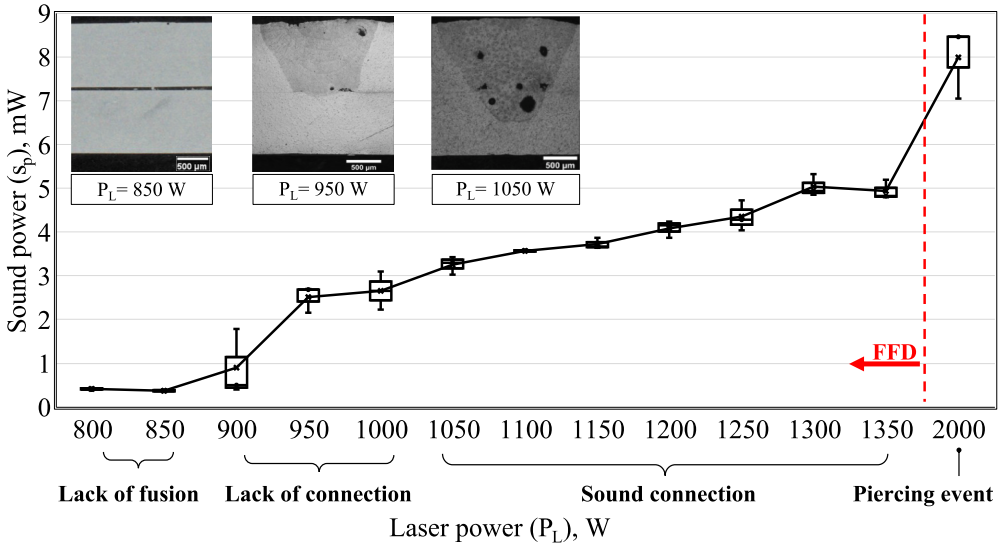

Fig. 7. Sound power (s_p) extracted from the ROI (all welds at zero part-to-part gap). "FFD" indicates the process window tested by the full factorial design. The selected cross-sections correspond to lack of fusion (850 W), lack of connection (950 W), and sound connection (1050 W).

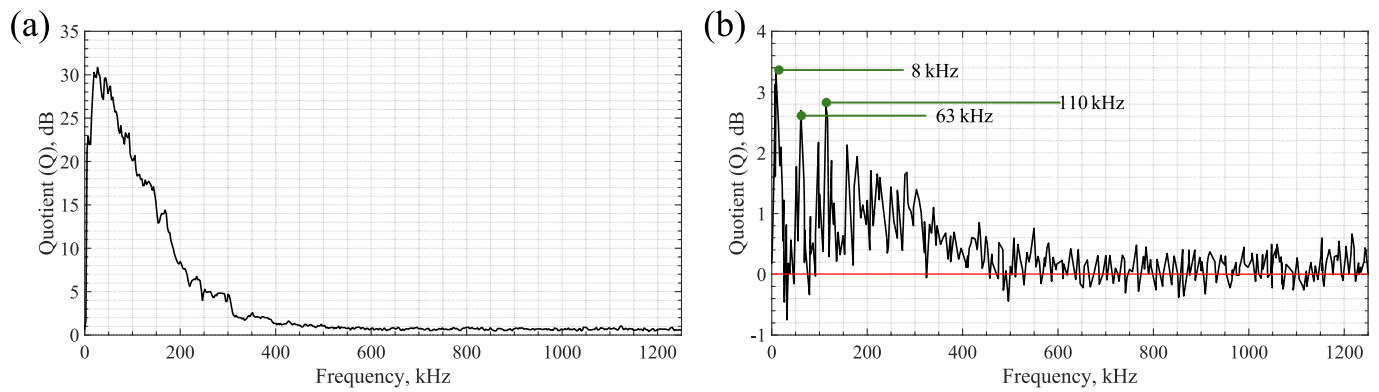

Fig. 8. (a) PSD quotient for P_L = [850, 950] W; (b) PSD quotient for P_L = [950, 1050] W (all welds at a zero part-to-part gap).

similar peak at $P_L = 1050$ W suggests that a stable keyhole likely begins to form. As the frequency increases beyond these peaks, the difference in the PSD quotient oscillates around zero, indicating that higher frequencies are less sensitive to changes in welding regime.

The peaks at 8 kHz and 110 kHz observed for the test at $P_L = 1050$ W, where both the upper and lower sheets are melted, indicate a slightly greater acoustic contribution at these frequencies compared to the test at P_L = 950 W, during which only the upper sheet is melted without penetration into the lower sheet. This may be explained by the fact that melting more material leads to a stronger resonance effect. Nevertheless, the authors recommend that future studies undertake a more detailed examination of these peaks.

3.2. *Detection of piercing event at zero part-to-part gap*

While the previous analysis described the progressive influence of increasing laser power over AE, a different phenomenon emerges when the process transitions from a blind to a passing-through keyhole, requiring separate evaluation. As shown in Fig. 9, the 8–26 kHz band is the only frequency range where at P_L = 2000 W the spectrum exceeds those at lower power levels. Across the remaining frequencies, the P_L = 2000 W spectrum falls below the $P_L = 1350$ W trace, which corresponds to full penetration without piercing. To analyze the AE's trend while excluding the 8–26 kHz range, a second-order Butterworth band-stop filter was applied, ensuring minimal distortion within the passband [39]. The sound power was then recalculated after filtering (indicated as $s_{p,filt}$) and the trend with the laser power (P_L) is shown in Fig. 10. Yet, results showed an increasing trend with increasing power, but at P_L = 2000 W the sound power exhibited a clear drop.

The drop can indicate that, with a passing-through keyhole, there is an alteration to the laser-material interaction and thus a decrease in AE, except within specific frequency bands. This drop may be associated with a reduction in absorbance, as noted in the literature [40], in relation to molten pool dynamics during the formation of a fully penetrating keyhole. In such cases, the material absorbs less energy, resulting in reduced vibrations and lower acoustic power across most frequency bands. This finding supports the idea that laser-induced vibrations decrease as the laser does pierce the bottom sheet, consistent with a transition from a blind to a passing-through keyhole regime [41]. Previous studies support this observation. Li et al. [42] reported a reduction in AE upon reaching excessive penetration (piercing condition), attributing this effect to the reduced confinement of vapor and plume, which are allowed to escape freely through the bottom of the weld. Wei et al. [43] obtained a similar trend and noted that, after variational mode decomposition, the amplitude of the sound in the 7.78–12.46 kHz band decreased markedly under excessive penetration (piercing condition)

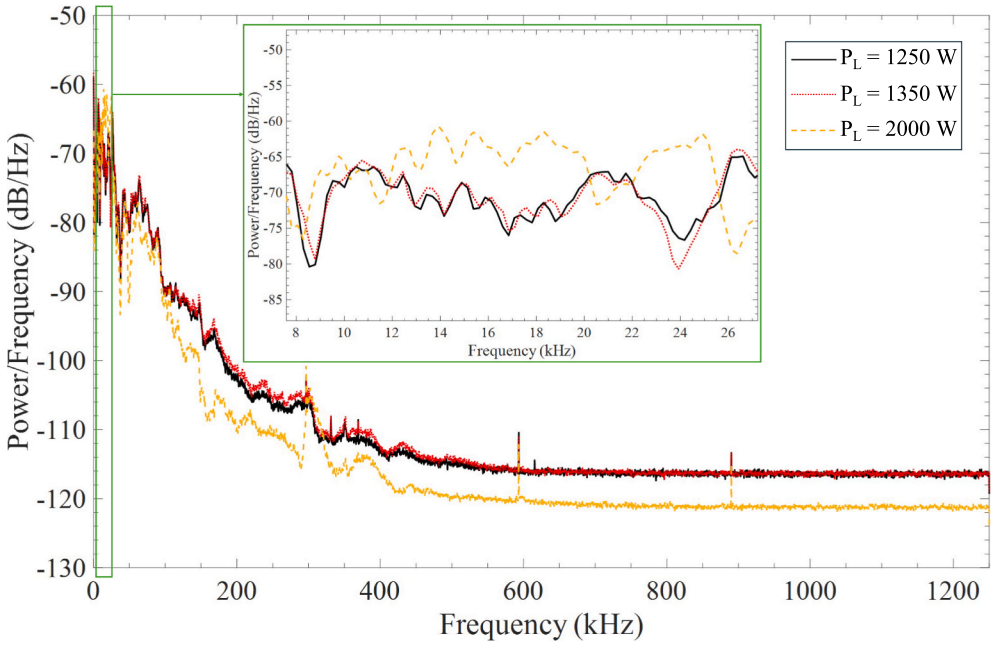

Fig. 9. PSD comparison for P_L = 1250, 1350, 2000 W (all welds at zero part-to-part gap). The zoom-in view shows the details of the PSD in the 8–26 kHz range.

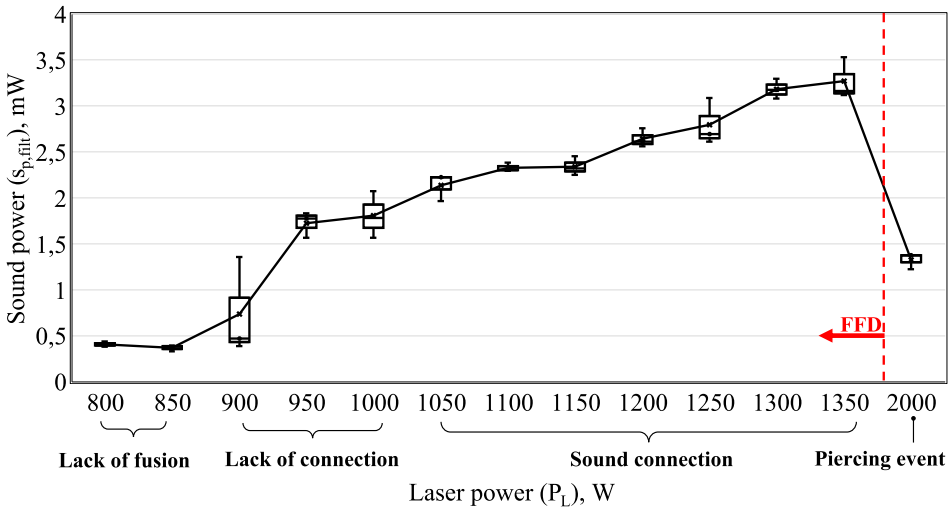

Fig. 10. Filtered sound power ($s_{p,filt}$) applying the 8–26 kHz band-stop filter (all welds at zero part-to-part gap). "FFD" indicates the process window tested by the full factorial design.

relative to under- and excessive-penetration welding. Studies on the optical emissions during excessive penetration welding reinforce this interpretation. Jie et al. [44] showed that the plume area, centroid height, and radiance contract once excessive penetration occurs, attributing this to the vapor venting through the underside so that the topside plume becomes smaller and cooler. Huang et al. [45] likewise reported an abrupt fall in electron temperature after the transition to over-penetration in Al–Mg arc welding, and Zhang et al. [46] observed the concomitant collapse of plume centroid height together with a redistribution of low-frequency dynamic content. The correlation between spectral and AE is particularly noteworthy. Luo et al. [47] concurrently measured plasma electron–temperature and both airborne and structure-borne acoustic signals and found that the three traces rise and fall together as the process shifts between conduction and keyhole regimes, demonstrating a direct correlation between plume dynamics and the emitted acoustic energy. Collectively, these observations indicate that keyhole breakthrough (piercing) leads to reduced energy absorption in the molten pool and decreased vapor activity above the surface, which in turn weakens both plume signatures and broadband acoustic emissions.

While the filtered signal reveals a general drop in broadband AE due to piercing, a distinct behavior is observed within the 8–26 kHz range, where the sound power instead increases with laser power. This contrasting trend suggests that additional mechanisms, separate from keyhole breakthrough, may be driving the acoustic activity in this specific frequency band. The increase in sound power in the 8–26 kHz band is likely influenced by other factors related to the laser-to-material interaction and discussed as follows:

- *Molten pool dynamics and vaporization*: with higher laser powers, the energy transferred to the material increases the molten pool's activity and accelerates vaporization. This results in more turbulent flow within the molten material and a higher rate of vapor release, both of which are likely contributors to the increased sound power in the 8–26 kHz range. The molten pool and vapor plume interactions generate acoustic emissions as they become more dynamic with increasing power [11];
- *Thermal expansion and contraction*: as the laser power intensifies, the thermal gradients within the material steepen, causing rapid thermal expansion and contraction. These thermal stresses are a likely source of acoustic emissions, particularly in the 8–26 kHz range. The material's thermal response, which intensifies with higher power, drives the generation of sound waves as the molten material rapidly heats and cools [42,48].

Therefore, while piercing attenuates broadband acoustic emissions due to reduced energy absorption, the 8–26 kHz band appears to capture residual or alternative laser-to-material interactions, highlighting its potential as a sensitive indicator for high-energy dynamics occurring during keyhole breakthrough. Further research should focus on validating whether the acoustic signatures observed during the piercing events are consistent across a broader range of materials and welding conditions.

3.3. *Variation of part-to-part gap*

This section investigates the influence of part-to-part gap on AE. For the sake of discussion, the metallographic analysis of two representative laser power levels is shown in Fig. 11 (a). At $P_L = 1150$ W, a connection occurred only for gap levels of 0, 0.25, and 0.5 mm, while no connection was achieved for the larger gaps. At $P_L = 1350$ W, a connection between the two parts was achieved for all gap levels except for the 1 mm gap.

The effectiveness of the weld connection is inherently tied to the interaction between the laser energy, molten pool dynamics, and gap size. Smaller gaps, such as 0 mm and 0.25 mm, promote efficient heat conduction between the upper and bottom sheets. This proximity allows for localized melting at the interface, leading to an effective connection. As the gap increases, the efficiency of heat transfer diminishes, resulting in incomplete fusion at the interface [49]. For gaps larger than 0.5 mm, the inability to bridge the gap with molten material results in the absence of a connection. At 1350 W, the higher laser power compensates for the increased gap by delivering more energy to the weld zone, enhancing the flow of the molten material. This increased energy facilitates the bridging of larger gaps (up to 0.75 mm) through capillary action and gravitational forces [50]. However, at the extreme gap of 1 mm, the molten pool's dynamics are insufficient to bridge the gap effectively, leading to lack of connection. To keep consistency with the findings discussed in Section 3.1, s_p was calculated from acoustic signals applying the 8–26 kHz band-stop filter. Fig. 11 (b) presents the variation of the filtered sound power ($s_{p,filt}$) as a function of part-to-part gap for the laser power levels that resulted in a sound connection at zero part-to-part gap (Fig. 10). A relatively strong negative correlation (Pearson's correlation coefficient = 79.7 %) was found between the part-to-part gap (across all the tested power levels) and $s_{p,filt}$. This result is significant since it shows that AE diminish as the gap increases. This correlation highlights the sensitivity of the acoustic signal to changes in interfacial conditions, as larger gap sizes facilitate venting at the sheet interface, allowing vapor and pressure to escape and thereby reducing plume confinement and the resulting acoustic energy [7,49].

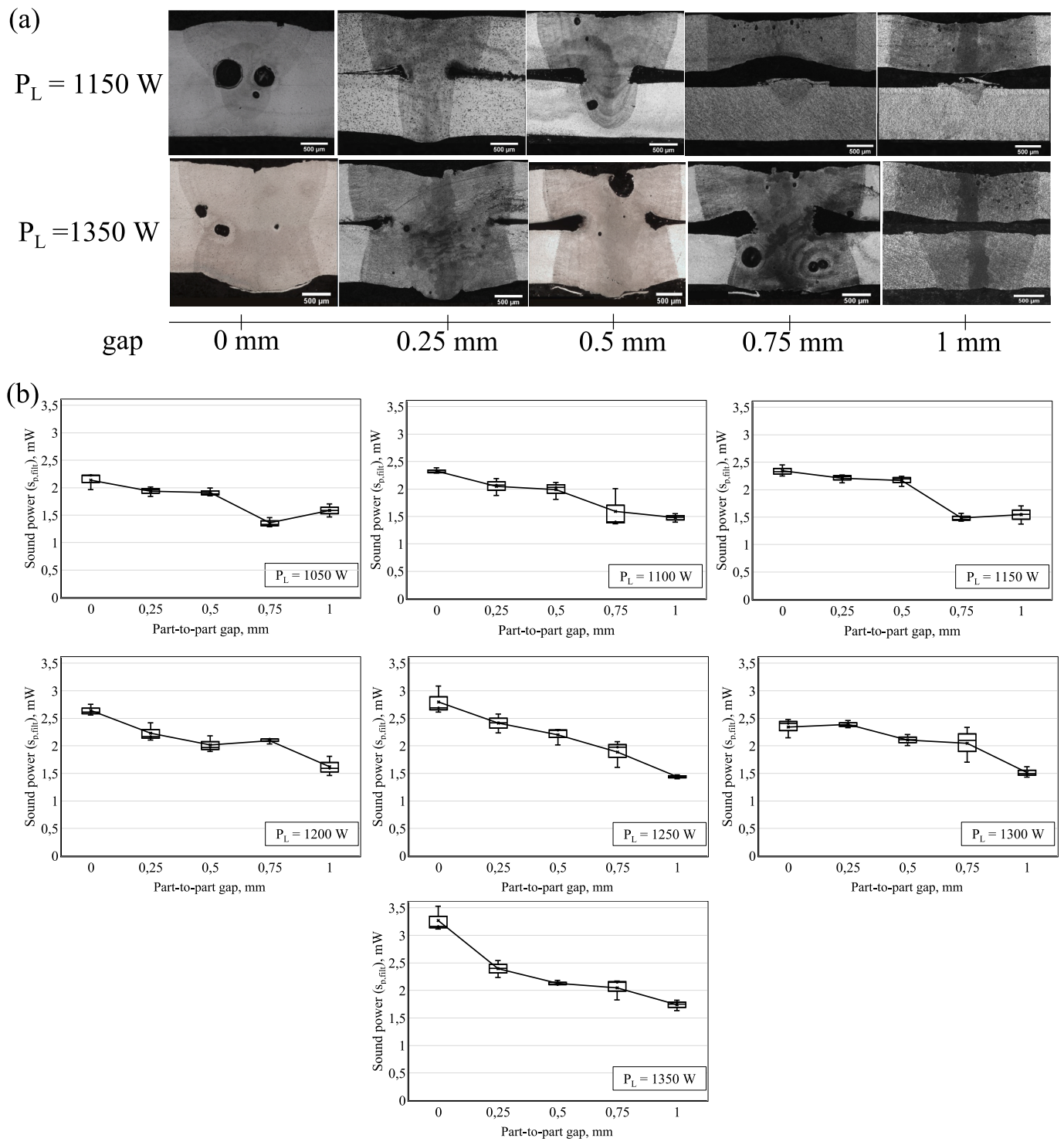

Fig. 11. (a) Macro-sections for P_L = 1150 and 1350 W at variable gap levels; (b) sound power ($s_{p,filt}$) applying the 8–26 kHz band-stop filter at varying part-to-part gap.

3.4. Combined effect of laser power and part-to-part gap

This section evaluates how the interaction between laser power and part-to-part gap influences AE and weld quality. Once again, to keep consistency with the findings discussed in previous sections, sound power was calculated from acoustic signals applying the 8–26 kHz band-stop filter (indicated as $s_{p,filt}$). To statistically quantify the combined influence of laser power and part-to-part gap on the acoustic emissions captured by the optical microphone, a two-way ANOVA was conducted. The rationale for employing this approach lies in its effectiveness in evaluating not only the individual effects of each factor, part-to-part gap (five levels: 0–1 mm) and laser power (P_L, twelve levels: 800–1350 W), but also their potential interactive effects on acoustic responses. These interactions are particularly critical, as the physics of the welding process suggests that variations in laser power may have different effects depending on the gap size, effects that cannot be fully captured through single-factor analyses alone. The ANOVA results, summarized in Table 5, demonstrate that both main factors and their interaction (p-

Table 5
Two-way ANOVA results of laser power, part-to-part gap and related interaction.

Source	df	Sum Sq	Mean Sq	F	p	Partial η^2
Part-to-part gap	4.0	0.06084	0.01521	31.99	<0.0001	0.42
P_L	11.0	0.32225	0.02930	61.57	<0.0001	0.73
Part-to-part gap × P_L	44.0	0.04879	0.00111	2.33	<0.0001	0.28
Residual	120.0	0.05714	0.00048			

vales below the 5 % significance level) significantly influence sound power ($s_{p,filt}$). The statistical effect sizes (η^2) indicate that laser power accounts for the largest portion of variability, followed by part-to-part gap, with a moderate yet statistically significant interaction effect.

Table 6 presents the marginal means, with 95 % Confidence intervals (CI), for each part-to-part gap level, averaged over all power levels. Notably, small part-to-part gap levels (0–0.5 mm) yield slightly higher $s_{p,filt}$ than higher part-to-part gap levels, while overall $s_{p,filt}$ remains in a relatively narrow range (approx. 0.05–0.06 mW). Generally, $s_{p,filt}$ increases with rising P_L, yielding a positive correlation of 82 % (Pearson's correlation coefficient), likely due to the intensified AE that result from greater energy input. This is in agreement with the findings presented in Section 3.1 for zero part-to-part gap. Interestingly, for smaller gaps (0.00 and 0.25 mm), $s_{p,filt}$ increases more steeply as the laser power rises (see Fig. 11(b)), implying that the proximity between the upper and lower sheet facilitates more effective heat transfer, amplifying the resulting acoustic emissions. Opposite to this, at larger gaps (0.75 and 1.00 mm), $s_{p,filt}$ does increase more gradually with the laser power. Additionally, for the same laser power, it is observed that, on average, $s_{p,filt}$ tends to decrease with the part-to-part gap. These observations are summarized as follows:

- *For* smaller gaps (<0.5 mm), the laser power is the dominating parameter that linearly correlates with the sound power.
- For larger gaps, the gap bridging is weakened, and hence a venting effect takes place at the part-to-part interface, attenuating the acoustic emissions. This is also in agreement with the results in [7].

Fig. 12 provides the summary of $s_{p,filt}$ across all combinations of laser power and gap levels evaluated in this study, visually reinforcing the trends discussed previously. It particularly highlights how AE consistently reflect the interplay between laser power intensity and part-to-part gap conditions. Notably, the variability indicated by the error bars emphasizes that certain parameter combinations, especially those near transition zones (e.g., intermediate power and gap levels), lead to less stable welding conditions and consequently higher variability in acoustic responses. Based on empirical analysis of the collected acoustic emission data, two distinct sound power ($s_{p,filt}$) thresholds were identified for classifying weld quality:

- A lower threshold of 0.5 mW effectively separates conditions of lack of fusion ($s_{p,filt} < 0.5$ mW) from those involving partial melting but insufficient connection (lack of connection, 0.5 mW < $s_{p,filt}$ < 1.8 mW).
- A higher threshold of 1.8 mW reliably distinguishes between lack of connection and stable, effective weld conditions (sound connection, $s_{p,filt} > 1.8$ mW).

Table 6
Marginal means of sound power by gap level with 95% CI.

Part-to-part gap	Mean $s_{p,filt}$	95 % CI Lower	95 % CI Upper
0.00	0.0548	0.0526	0.0570
0.25	0.0579	0.0558	0.0601
0.50	0.0607	0.0585	0.0629
0.75	0.0534	0.0513	0.0555
1.00	0.0541	0.0520	0.0562

While these thresholds provide a useful acoustic criterion for weld quality classification, it is important to note that borderline cases near the threshold – particularly between lack of connection and sound connection – may still lead to misclassifications. This is likely due to overlapping acoustic features or subtle variations in weld morphology not fully captured by sound power alone. Further research should focus on refining this classification by exploring advanced signal processing techniques, including machine learning algorithms or sensor data fusion, to improve robustness and classification accuracy under varying process conditions.

3.5. Summary of observed cause-effect phenomena

The key findings are summarized in Table 7, highlighting the relationship between laser power, part-to-part gap, and the corresponding welding phenomena and AE.

The observed variations in the acoustic emissions recorded by the optical microphone are strongly influenced by the interplay between laser power, part-to-part gap, and the resulting keyhole and melt pool dynamics. At low laser powers ($P_L < 800$ W), insufficient energy delivery leads to a lack of fusion, manifesting as low amplitude acoustic signals. This is consistent with previous studies, which show that minimal melting events produce weak pressure fluctuations and thus limited acoustic activity [27]. As the laser power increases and exceeds the melting threshold (P_L = 1050 – 1350 W), the formation of a stable keyhole and dynamic melt pool oscillations is accompanied by a pronounced increase in both the amplitude and the frequency content of the acoustic signal. The appearance of characteristic peaks, such as at 63 kHz, is likely attributable to the resonant oscillation of the keyhole cavity, as reported in earlier work [9,28]. With further laser power increases (P_L = 2000 W), the transition from a blind to a passing-through keyhole (piercing) is marked by a sharp decrease in broadband acoustic emissions after application of a band-stop filter, in agreement with the venting hypothesis advanced by [42,43]. The formation of a fully open channel reduces pressure confinement in the molten pool, allowing vapor and plume to escape downward, which in turn diminishes acoustic and optical emission above the weld [44]. Notably, this venting effect produces similar acoustic attenuation to that observed for excessive part-to-part gap, underlining that loss of confinement is a common mechanism across distinct process faults. The response of the acoustic signal to variations in gap size can be similarly rationalized. Small to moderate gaps (up to 0.5 mm) maintain interfacial coupling, facilitating heat transfer and stable melt pool dynamics, which are detected as high-amplitude, oscillatory AE. At larger gaps (>0.50 mm), the interface acts as a vent, dispersing vapor and suppressing both the amplitude and variability of the signal, in line with findings from computational fluid dynamics and experimental studies [7,49].

From a monitoring perspective, these results demonstrate the feasibility of using membrane-free optical microphones for real-time detection of critical weld conditions, particularly transitions associated with defective fusion or dangerous piercing events. The strong correlation between acoustic emissions and weld quality observed here provides a quantitative foundation for the development of robust in-process monitoring and control strategies, although further research is warranted to address industrial implementation challenges such as ambient noise and process variability.

4. Conclusions and final remarks

This study evaluated the effectiveness of a membrane-free optical microphone in detecting weld events – lack of fusion, lack of connection, sound connection, and piercing – arising from changes in part-to-

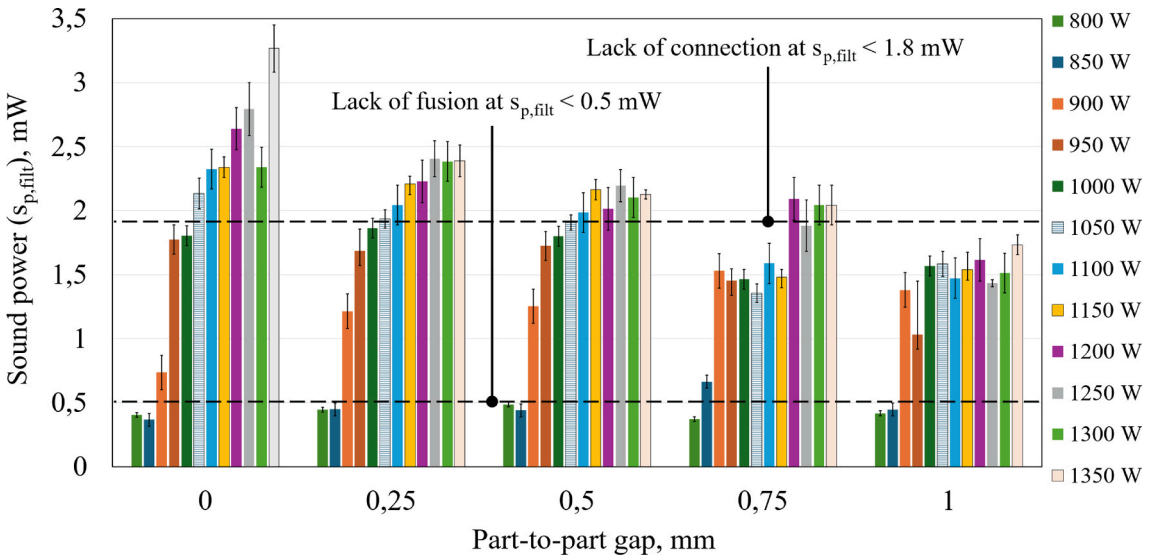

Fig. 12. Sound power ($s_{p,filt}$) applying the 8–26 kHz band-stop filter, shown for all combinations of laser power (800–1350 W) and part-to-part gap (0–1 mm).

Table 7
Summary of welding events and corresponding cause-effects observed during laser welding of 1 mm 1050 aluminum.

Event	Cause	Effect
Lack of Fusion	Low laser power (< 0.8 kW)	– No melting; only surface marking – $s_{p,filt}$ < 0.5 mW across the whole spectrum after applying the 8–26 kHz band-stop filter
Lack of Connection	– Low laser power (< 1 kW) – Large part-to-part gap (> 0.75 mm)	– Weak or unstable melt pool dynamics – Attenuation of the acoustic emissions through the part-to-part gap interface – s_p drops below 1.8 mW after applying the 8–26 kHz band-stop filter
Sound Connection	– Adequate laser power (1–1.3 kW) – Small/medium gap (< 0.75 mm)	– Effective and stable weld fusion – $s_{p,filt}$ > 1.8 mW – Frequency peak at 63 kHz reflects stable keyhole dynamics
Piercing	Excessive laser power (> 2000 W)	– Transition to a fully passing-through keyhole reduces laser absorptance resulting in decreased acoustic emissions – $s_{p,filt}$ drops below 1.8 mW

part gaps and laser power. The investigation focused on the laser welding of 1 mm 1050 aluminum, representative of busbar-to-terminal connections in battery modules.

A key contribution of this work is the demonstration of the microphone's ability to diagnose the transition from a blind to a passing-through keyhole, triggered by laser piercing events. At a laser power of 2000 W, where penetration of the bottom sheet occurred, a noticeable drop in sound power was detected after applying a second-order band-stop filter. This enabled clear identification of the piercing defect, an essential capability for avoiding damage to critical components during battery manufacturing.

To isolate the influence of laser power and part-to-part gap, the study deliberately excluded the use of a cross-jet. Future research will investigate the microphone's performance in configurations that include cross-jets, thereby enabling assessment under conditions more representative of real-world production environments. Furthermore, additional research is needed to rigorously quantify the microphone's performance in noisy industrial settings. Specifically, future studies should systematically evaluate the sensor's sensitivity to varying types and levels of background noise and explore advanced noise-mitigation techniques to fully validate its practical advantages.

By linking distinct acoustic signatures to weld events, the study establishes a strong foundation for real-time weld defect detection in laser welding. It is important to note that this study primarily presented evidence of correlations between acoustic emissions and weld events, rather than a fully deployed real-time defect detection system. Nonetheless, the identification of acoustic thresholds shows promising potential for the development of decision rules for real-time defect classification. Realizing practical implementation in industrial environments will require further research into robust real-time signal processing, sensor calibration, and noise suppression strategies. Future efforts should focus on translating the correlation-based findings into operational monitoring systems, with emphasis on real-time signal analysis and addressing the challenges of deployment in complex, high-noise manufacturing settings.

CRediT authorship contribution statement

Dario Basile: Writing – original draft, Visualization, Methodology, Investigation, Formal analysis, Data curation, Conceptualization. **Rehab Al Botros:** Supervision, Methodology. **Manuela De Maddis:** Writing – review & editing, Supervision. **Valentino Razza:** Writing – review & editing. **Pasquale Franciosa:** Writing – review & editing, Visualization, Supervision, Resources, Project administration, Methodology, Conceptualization.

Declaration of competing interest

The authors declare that they have no known competing financial interests or personal relationships that could have appeared to influence the work reported in this paper.

Acknowledgments

We greatly acknowledge the support of the Student Exchange Program between Politecnico di Torino and University of Warwick. P. Franciosa also acknowledges the financial support of (1) WMG HVM Catapult; (2) Lasers for Accelerated Net-Zero Transition (Laser4NetZero - grant agreement 101119711); (3) Laser-as-a-Service Digital Platform with Dynamic Beam Shaping for Acceleration of Smart, Decentralised and Sustainable Factory of the Future (Lasers4MaaS - grant agreement 101178719).

Data availability

The data and information that support the findings of this article are freely available (10.5281/zenodo.15833960).

References

[1] J. Jaguemont, F. Bardé, A critical review of lithium-ion battery safety testing and standards, Appl. Therm. Eng. 231 (2023) 121014, https://doi.org/10.1016/J.APPLTHERMALENG.2023.121014.

[2] J. Feng, P. Zhang, H. Yan, H. Shi, Q. Lu, Z. Liu, D. Wu, T. Sun, R. Li, Q. Wang, Application of laser welding in electric vehicle battery manufacturing: A review, Coatings 13 (2023) (2023) 1313, https://doi.org/10.3390/COATINGS13081313.

[3] M.F.R. Zwicker, M. Moghadam, W. Zhang, C.V. Nielsen, Automotive battery pack manufacturing – A review of battery to tab joining, J. Adv. Joining Process. 1 (2020) 100017, https://doi.org/10.1016/J.JAJP.2020.100017.

[4] G. May, D. Kiritsis, Zero defect manufacturing strategies and platform for smart factories of industry 4.0, Lecture Notes Mech. Eng. (2019) 142–152, https://doi.org/10.1007/978-3-030-18180-2_11/FIGURES/4.

[5] W. Cai, J.Z. Wang, P. Jiang, L.C. Cao, G.Y. Mi, Q. Zhou, Application of sensing techniques and artificial intelligence-based methods to laser welding real-time monitoring: A critical review of recent literature, J. Manuf. Syst. 57 (2020) 1–18, https://doi.org/10.1016/J.JMSY.2020.07.021.

[6] M. Sokolov, P. Franciosa, T. Sun, D. Ceglarek, V. Dimatteo, A. Ascari, A. Fortunato, F. Nagel, Applying optical coherence tomography for weld depth monitoring in remote laser welding of automotive battery tab connectors, J. Laser Appl. 33 (2021), https://doi.org/10.2351/7.0000336/989783.

[7] G. Chianese, P. Franciosa, J. Nolte, D. Ceglarek, S. Patalano, Characterization of photodiodes for detection of variations in part-to-part gap and weld penetration depth during remote laser welding of copper-to-steel battery tab connectors, J. Manuf. Sci. Eng., Trans. ASME 144 (2022), https://doi.org/10.1115/1.4052725/1121743.

[8] M.F.M. Yusof, M. Ishak, M.F. Ghazali, Acoustic methods in real-time welding process monitoring: Application and future potential advancement, J. Mech. Eng. Sci. 15 (2021) 8490–8507, https://doi.org/10.15282/jmes.15.4.2021.03.0669.

[9] N. Authier, E. Touzet, F. Lücking, R. Sommerhuber, V. Bruyere, P. Namy, Coupled membrane free optical microphone and optical coherence tomography keyhole measurements to setup welding laser parameters, SPIE-Intl Soc Optical Eng (2020) 8, https://doi.org/10.1117/12.2543999.

[10] B. Fischer, Optical microphone hears ultrasound, Nat. Photonics 10 (2016) 356–358, https://doi.org/10.1038/NPHOTON.2016.95.

[11] T. Klein, M. Vicanek, J. Kroos, I. Decker, G. Simon, Oscillations of the keyhole in penetration laser beam welding, J. Phys. D Appl. Phys. 27 (1994) 2023, https://doi.org/10.1088/0022-3727/27/10/006.

[12] M. Geiger, K.H. Leitz, H. Koch, A. Otto, A 3D transient model of keyhole and melt pool dynamics in laser beam welding applied to the joining of zinc coated sheets, Prod. Eng. 3 (2009) 127–136, https://doi.org/10.1007/S11740-008-0148-7/FIGURES/9.

[13] J. Volpp, D. Freimann, Indirect measurement of keyhole pressure oscillations during laser deep penetration welding, ICALEO 2013 - 32nd International Congress on, Appl. Lasers Electro-Opt. (2013) 334–340, https://doi.org/10.2351/1.5062896/847302.

[14] K. Schricker, L. Schmidt, H. Friedmann, C. Diegel, M. Seibold, P. Hellwig, F. Fröhlich, J.P. Bergmann, F. Nagel, P. Kallage, A. Rack, Characterization of keyhole dynamics in laser welding of copper by means of high-speed synchrotron X-ray imaging, Procedia CIRP 111 (2022) 501–506, https://doi.org/10.1016/j.procir.2022.08.079.

[15] Z. Luo, L. Shu, P. Jiang, S. Geng, D. Ma, D. Wu, Study on the keyhole oscillation mechanism of laser welding based on electro-mechano-acoustical analogy theory, J. Mater. Process. Technol. 331 (2024), https://doi.org/10.1016/j.jmatprotec.2024.118495.

[16] Y. Luo, L. Zhu, J. Han, X. Xie, R. Wan, Y. Zhu, Study on the acoustic emission effect of plasma plume in pulsed laser welding, Mech. Syst. Signal Process. 124 (2019) 715–723, https://doi.org/10.1016/j.ymssp.2019.01.045.

[17] M. Bastuck, In-Situ-Überwachung von Laserschweißprozessen mittels höherfrequenter Schallemissionen, (2016). https://doi.org/10.22028/D291-23167.

[18] M. Hamidi Nasab, G. Masinelli, C. de Formanoir, L. Schlenger, S. Van Petegem, R. Esmaeilzadeh, K. Wasmer, A. Ganvir, A. Salminen, F. Aymanns, F. Marone, V. Pandiyan, S. Goel, R.E. Logé, Harmonizing sound and light: X-ray imaging unveils acoustic signatures of stochastic inter-regime instabilities during laser melting, Nat. Commun. 14 (2023), https://doi.org/10.1038/s41467-023-43371-3.

[19] C. de Formanoir, M. Hamidi Nasab, L. Schlenger, S. Van Petegem, G. Masinelli, F. Marone, A. Salminen, A. Ganvir, K. Wasmer, R.E. Logé, Healing of keyhole porosity by means of defocused laser beam remelting: Operando observation by X-ray imaging and acoustic emission-based detection, Addit. Manuf. 79 (2024) 103880, https://doi.org/10.1016/J.ADDMA.2023.103880.

[20] C. Prieto, R. Fernandez, C. Gonzalez, M. Diez, J. Arias, R. Sommerhuber, F. Lücking, In situ process monitoring by optical microphone for crack detection in Laser Metal Deposition applications, 2020.

[21] C. Lutz, C. Esen, R. Hellmann, Layer detection in ultrashort pulsed multilayer laser ablation by analyzing ultrasonic process emission, J. Laser Appl. 37 (2025), https://doi.org/10.2351/7.0001740.

[22] C. Lutz, R. Sommerhuber, M. Kettner, C. Esen, R. Hellmann, Towards process control by detecting acoustic emissions during ultrashort pulsed laser ablation of multilayer materials, in, SPIE-Intl Soc Optical Eng (2024) 51, https://doi.org/10.1117/12.3000954.

[23] Andreas Krämer, Influence of the airborne sound sensor position on the detectability of acoustic emissions during deep penetration laser welding, (2024). https://doi.org/10.48446/opus-14791.

[24] M. Omlor, J. Reith, A. Breitbarth, C.B. Hake, K. Dilger, Inline Process Monitoring of Hairpin Welding Using Optical and Acoustic Quality Metrics, in: 2022 12th International Electric Drives Production Conference, EDPC 2022 - Proceedings, Institute of Electrical and Electronics Engineers Inc., 2022. https://doi.org/10.1109/EDPC56367.2022.10019745.

[25] J. Heilmeier, M.K. Kick, S. Grabmann, T. Muschol, F. Schlicht, F. von Hundelshausen, H.-G. von Ribbeck, T. Weiss, M.F. Zaeh, Inline failure detection in laser beam welding of battery cells: Acoustic and spectral emission analysis for quality monitoring, J. Laser Appl. 36 (2024), https://doi.org/10.2351/7.0001216.

[26] A. Krämer, I. Henze, R. Pordzik, T. Radel, Inline detection of process anomalies during laser deep penetration welding of hidden T-joints, Procedia CIRP (2024) 526–529, https://doi.org/10.1016/j.procir.2024.08.167.

[27] T. Weiss, J. Werner, C. Geiger, M.F. Zaeh, Acoustic process monitoring during the laser beam welding of stainless-steel foils using an adjustable ring mode laser beam source, J. Laser Appl. 36 (2024), https://doi.org/10.2351/7.0001575.

[28] L. Tomcic, A. Ederer, S. Grabmann, M. Kick, J. Kriegler, M.F. Zaeh, Interpreting acoustic emissions to determine the weld depth during laser beam welding, J. Laser Appl. 34 (2022), https://doi.org/10.2351/7.0000796.

[29] C. Geiger, P. Garkusha, C. Bernauer, S. Mehrl, P.A. Schirmer, M.F. Zaeh, Acoustic process monitoring during the structuring of the diffusion media for fuel cells with Ultrashort Laser Pulses, Procedia CIRP 124 (2024) 51–56, https://doi.org/10.1016/J.PROCIR.2024.08.069.

[30] S. Shahid, M. Agelin-Chaab, A review of thermal runaway prevention and mitigation strategies for lithium-ion batteries, Energy Convers. Manage.: X 16 (2022) 100310, https://doi.org/10.1016/J.ECMX.2022.100310.

[31] C.E. Shannon, Communication in the Presence of Noise, Proceedings of the I.R.E. (1949). https://doi.org/10.1109/JRPROC.1949.232969.

[32] T. Sun, P. Franciosa, D. Ceglarek, Effect of focal position offset on joint integrity of AA1050 battery busbar assembly during remote laser welding, J. Mater. Res. Technol. 14 (2021) 2715–2726, https://doi.org/10.1016/J.JMRT.2021.08.002.

[33] S. Arzanpour, J. Fung, J.K. Mills, W.L. Cleghorn, Flexible fixture design with applications to assembly of sheet metal automotive body parts, Assem. Autom. 26 (2006) 143–153, https://doi.org/10.1108/01445150610658130/FULL/PDF.

[34] T. Ji, N. Mohamad Nor, Deep learning-empowered digital twin using acoustic signal for welding quality inspection, Sensors 23 (2023), https://doi.org/10.3390/s23052643.

[35] W. Huang, R. Kovacevic, Acoustic monitoring of weld penetration during laser welding of high strength steels, ICALEO 2009–28th International Congress on applications of Lasers and Electro-Optics, Cong. Proc. 102 (2009) 630–637, https://doi.org/10.2351/1.5061620/1003956.

[36] A. V. Oppenheim, Discrete-time signal processing, Third edition., Pearson, Upper Saddle River N.J, 2010. https://doi.org/10.5555/294797.

[37] P.D. Welch, The use of fast fourier transform for the estimation of power spectra: A method based on time averaging over short, modified periodograms, IEEE Trans. Audio Electroacoust. 15 (1967) 70–73, https://doi.org/10.1109/TAU.1967.1161901.

[38] A. V. Oppenheim, Discrete-time signal processing, Third edition., Pearson, Upper Saddle River N.J, 2010.

[39] Standard Responses, Op Amp Applications Handbook (2005) 325–348. https://doi.org/10.1016/B978-075067844-5/50137-5.

[40] A. Blug, F. Abt, L. Nicolosi, A. Heider, R. Weber, D. Carl, H. Höfler, R. Tetzlaff, The full penetration hole as a stochastic process: Controlling penetration depth in keyhole laser-welding processes, Appl. Phys. B 108 (2012) 97–107, https://doi.org/10.1007/s00340-012-5104-8.

[41] J. Wagner, C. Hagenlocher, R. Weber, T. Graf, The change of the absorptance at the transition from partial- to full-penetration laser welding, Int. J. Adv. Manuf. Technol. 134 (2024) 497–509, https://doi.org/10.1007/S00170-024-14075-9/FIGURES/12.

[42] L. Li, W.M. Steen, Non-contact acoustic emission monitoring during laser processing, in: LIA (Laser Institute of America), Publ by Laser Inst of America, 1993: pp. 719–728. https://doi.org/10.2351/1.5058543.

[43] W. Wei, Q. Kong, G. He, H. Li, J. Ren, N. Deng, Z. Chen, Y. Long, A novel monitoring method based on the fusion of sound and image signals for laser welding penetration status, Proc. Inst. Mech. Eng. B J. Eng. Manuf. (2024), https://doi.org/10.1177/09544054241289468.

[44] J. Li, Y. Zhang, W. Liu, B. Li, X. Yin, C. Chen, Prediction of penetration based on plasma plume and spectrum characteristics in laser welding, J. Manuf. Process. 75 (2022) 593–604, https://doi.org/10.1016/J.JMAPRO.2022.01.032.

[45] Y. Huang, S. Li, J. Li, H. Chen, L. Yang, S. Chen, Spectral diagnosis and defects prediction based on ELM during the GTAW of Al alloys, Measurement 136 (2019) 405–414, https://doi.org/10.1016/J.MEASUREMENT.2018.12.074.

[46] Y. Zhang, F. Li, Z. Liang, Y. Ying, Q. Lin, H. Wei, Correlation analysis of penetration based on keyhole and plasma plume in laser welding, J. Mater. Process. Technol. 256 (2018) 1–12, https://doi.org/10.1016/J.JMATPROTEC.2018.01.032.

[47] Y. Luo, L. Zhu, J. Han, J. Xu, C. Zhang, D. Chen, Effect of focusing condition on laser energy absorption characteristics in pulsed laser welding, Opt. Laser Technol. 117 (2019) 52–63, https://doi.org/10.1016/J.OPTLASTEC.2019.04.001.

[48] R.D. Rawlings, W.M. Smen, Acoustic emission monitoring of surface hardebing by laser, 1981. https://doi.org/10.1016/0143-8166(81)90018-X.
[49] G. Chianese, S. Jabar, P. Franciosa, D. Ceglarek, S. Patalano, A multi-physics CFD study on the part-to-part gap during remote laser welding of copper-to-steel battery tab connectors with beam wobbling, in: Procedia CIRP, Elsevier B.V., 2022: pp. 484–489. https://doi.org/10.1016/j.procir.2022.08.075.
[50] P. Franciosa, A. Serino, R. Al Botros, D. Ceglarek, Closed-loop gap bridging control for remote laser welding of aluminum components based on first principle energy and mass balance, J. Laser Appl. 31 (2019), https://doi.org/10.2351/1.5096099.